Volume 12
Number 48
28 December 2021
Pages 15779–16124

Chemical Science

rsc.li/chemical-science

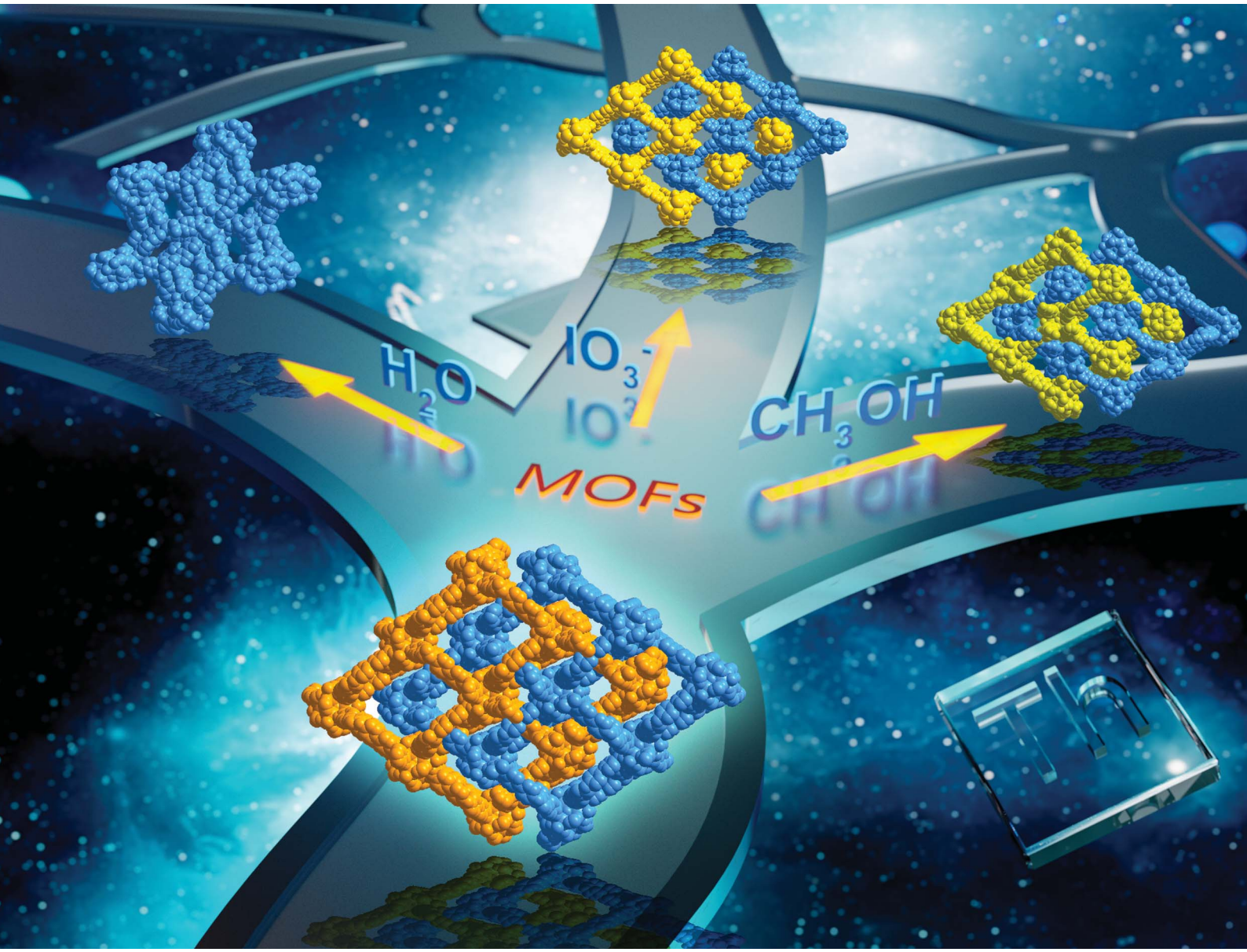

ISSN 2041-6539

ROYAL SOCIETY OF CHEMISTRY

EDGE ARTICLE

Jian-Qiang Wang, Wei Liu, Jian Lin *et al.*

A cationic thorium–organic framework with triple single-crystal-to-single-crystal transformation peculiarities for ultrasensitive anion recognition

Chemical Science

ROYAL SOCIETY OF CHEMISTRY

EDGE ARTICLE

View Article Online
View Journal | View Issue

Check for updates

Cite this: *Chem. Sci.*, 2021, **12**, 15833

All publication charges for this article have been paid for by the Royal Society of Chemistry

Received 8th July 2021
Accepted 20th October 2021

DOI: 10.1039/d1sc03709a

rsc.li/chemical-science

Open Access Article. Published on 20 October 2021. Downloaded on 5/3/2026 9:02:40 PM.
This article is licensed under a Creative Commons Attribution-NonCommercial 3.0 Unported Licence.

A cationic thorium–organic framework with triple single-crystal-to-single-crystal transformation peculiarities for ultrasensitive anion recognition†

Zi-Jian Li, ‡[a] Min Lei,‡[b] Hongliang Bao,‡[a] Yu Ju,[ad] Huangjie Lu,[a] Yongxin Li,[e] Zhi-Hui Zhang,[d] Xiaofeng Guo,[f] Yuan Qian,[a] Ming-Yang He,[d] Jian-Qiang Wang,*[a] Wei Liu*[b] and Jian Lin*[ac]

Single-crystal-to-single-crystal transformation of metal–organic frameworks has been met with great interest, as it allows for the creation of new materials in a stepwise manner and direct visualization of structural transitions when subjected to external stimuli. However, it remains a peculiarity among numerous metal–organic frameworks, particularly for the ones constructed from tetravalent metal cations. Herein, we present a cationic thorium–organic framework displaying unprecedented triple single-crystal-to-single-crystal transformations in organic solvents, water, and $NaIO_3$ solution. Notably, both the interpenetration conversion and topological change driven by the SC–SC transformation have remained elusive for thorium–organic frameworks. Moreover, the single-crystal-to-single-crystal transition in $NaIO_3$ solution can efficiently and selectively turn the ligand-based emission off, leading to the lowest limit of detection (0.107 μg kg^{-1}) of iodate, one of the primary species of long-lived fission product ^{129}I in aqueous medium, among all luminescent sensors.

Introduction

Metal–organic frameworks (MOFs) showing structural transformations and a corresponding characteristic response upon external stimuli are essential for their applications in chemosensing, switching, ion exchange, gas storage, *etc.*[1–5] As a unique type of structural evolution, single-crystal-to-single-crystal (SC–SC) transformation is particularly intriguing, as it allows creation of new materials and postsynthetic functionalization of MOFs in a stepwise and visualizable manner.[6–10] Furthermore, the mechanisms of gas uptake, ion exchange, sensing, *etc.* can be directly visualized at the molecular level *via* successive single-crystal X-ray diffraction (SCXRD).[11–14] However, SC–SC transformation remains a relatively uncommon peculiarity among the numerous numbers of existing MOFs, especially for the ones composed of tetravalent metal ions or clusters.[15–19] This is partially because the strong Lewis acidity of M^{4+} cations and, correspondingly, robust metal–ligand coordination not only make bond cleavage and formation rather challenging, but also make the crystallinity hard to retain.[20] In addition, most reported SC–SC transformations of tetravalent metal-based MOFs involve framework breathing, transmetallation, linker installation, and guest exchange, while topological transition and interpenetration conversion seldom occur.[15–19,21]

As the largest and "softest" tetravalent cation, Th^{4+} is least susceptible to hydrolysis and precipitation during self-assembly. This unique feature makes obtaining high quality single crystals of thorium–organic frameworks (TOFs) more accessible than the Zr, Hf, and Ce analogues in terms of crystal size and crystallinity.[22–25] Such properties are beneficial for constructing MOFs with capacities of SC–SC transformation because both the parental carriers and transformed phases can be structurally elucidated by SCXRD. Furthermore, the relatively weak node–linker interaction could make topology transformation, which involves cleavage and regeneration of bonds, less difficult than for the other tetravalent metal based MOFs.[26–29] Moreover, many structures of TOFs, *e.g.* $(Th_2F_5)(-NC_7H_5O_4)_2(H_2O)][NO_3]$, $[Th_3(bptc)_3O(H_2O)_{3.78}]Cl\cdot(C_5H_{14}N_3Cl)\cdot 8H_2O$ (SCU-8), and $[Th(L)\text{-}(H_2O)_2]\cdot 5.5DMF\cdot 4(H_2O)$ (SCU-11),

[a]*Shanghai Institute of Applied Physics, Chinese Academy of Sciences, Shanghai 201800, China. E-mail: wangjianqiang@sinap.ac.cn*
[b]*School of Environmental and Material Engineering, Yantai University, Yantai 264005, P. R. China. E-mail: wliu@ytu.edu.cn*
[c]*School of Nuclear Science and Technology, Xi'an Jiaotong University, No. 28, Xianning West Road, Xi'an, 710049, P. R. China. E-mail: jianlin@xjtu.edu.cn*
[d]*Jiangsu Key Laboratory of Advanced Catalytic Materials and Technology, Changzhou University, Changzhou 213164, China*
[e]*Division of Chemistry and Biological Chemistry, School of Physical and Mathematical Sciences, Nanyang Technological University, 637371, Singapore*
[f]*Department of Chemistry and Alexandra Navrotsky Institute for Experimental Thermodynamics, Washington State University Pullman, WA 99164-4630, USA*

† Electronic supplementary information (ESI) available: Characterization, FTIR, PXRD, N_2 sorption isotherms, TGA, quantum yields, excitation and PL spectra, PL lifetimes, SEM-EDS, proposed quenching mechanism, and crystallographic data. CCDC 2065485–2065488. For ESI and crystallographic data in CIF or other electronic format see DOI: 10.1039/d1sc03709a

‡ These authors contributed equally to this work.

© 2021 The Author(s). Published by the Royal Society of Chemistry

Open Access Article. Published on 20 October 2021. Downloaded on 5/3/2026 9:02:40 PM. This article is licensed under a Creative Commons Attribution-NonCommercial 3.0 Unported Licence.

which are built from monomeric Th^{4+} cations or unique secondary building units (SBUs), have not been reproduced by the well-studied Zr-MOFs.[30–34] However, there are only a few pioneering studies by Shustova *et al.* showing SC–SC transformation of TOFs *via* metal node substitution.[35,36] In addition, Th^{4+} and its high-nuclearity Th_6 cluster are of higher charge density and connectivity compared with low valent metal cations. This feature can promote the construction of cationic MOFs, a small fraction of the MOF family, which further makes the chemistry of TOFs worth exploring.[30,31,37,38]

Photoluminescent (PL) MOFs together with SC–SC transformation offer the opportunity for creating chemosensors for ion recognition, due to their dynamic frameworks and switchable emission feature upon host–guest interactions.[39,40] Guided by this strategy, we are particularly interested in developing novel TOF-based chemosensors for detecting radionuclide anions. As a predominant fission product, the long-lived ^{129}I ($t_{1/2} = 1.57 \times 10^7 y$) is of great concern, due to the excessive inventory, high mobility, bioaccumulation, and large contribution (13%) to the population dose.[41] Iodate (IO_3^-) accounts for up to 84% of the total ^{129}I present in the groundwater of the Hanford site and has been recognized as the culprit of nearby groundwater contamination.[42,43] Consequently, numerous types of instrumental analysis techniques have been developed, allowing for quantification of iodate down to 0.015 μg kg^{-1}.[44] Unfortunately, sophisticated sample pretreatment and instrument reliance make fast analysis and on-site monitoring of iodate rather unlikely. Chemosensors show merits in terms of portability and accessibility; however, the ones reported to date suffer from a lack of sufficient sensitivity and selectivity, which are key drawbacks for real-life applications.[45–47] Therefore, sensitive, selective, and facile detection of iodate in aqueous media is highly desired.

In this work, we showcase an extremely rare case of TOF, $[Th_6(\mu_3\text{-}OH)_8(H_2O)_3(DMF)(TCBPA)_4(HCOO)_2]\cdot(NO_3)_2$ (namely **Th-SINAP-200**), which undergoes SC–SC transformations to three distinct phases upon immersion in a variety of organic solvents, water, and iodate solution, *via* modifying its interpenetration and/or coordination environment of SBUs. To the best of our knowledge, neither the interpenetration conversion nor SC–SC transformation with topological transition has been reported for TOFs. Notably, the cationic framework and strong ligand-based emission of **Th-SINAP-200**, together with its SC–SC transformation in iodate solution allow for highly selective detection of iodate with a limit of detection (LOD) of 0.107 μg kg^{-1}.

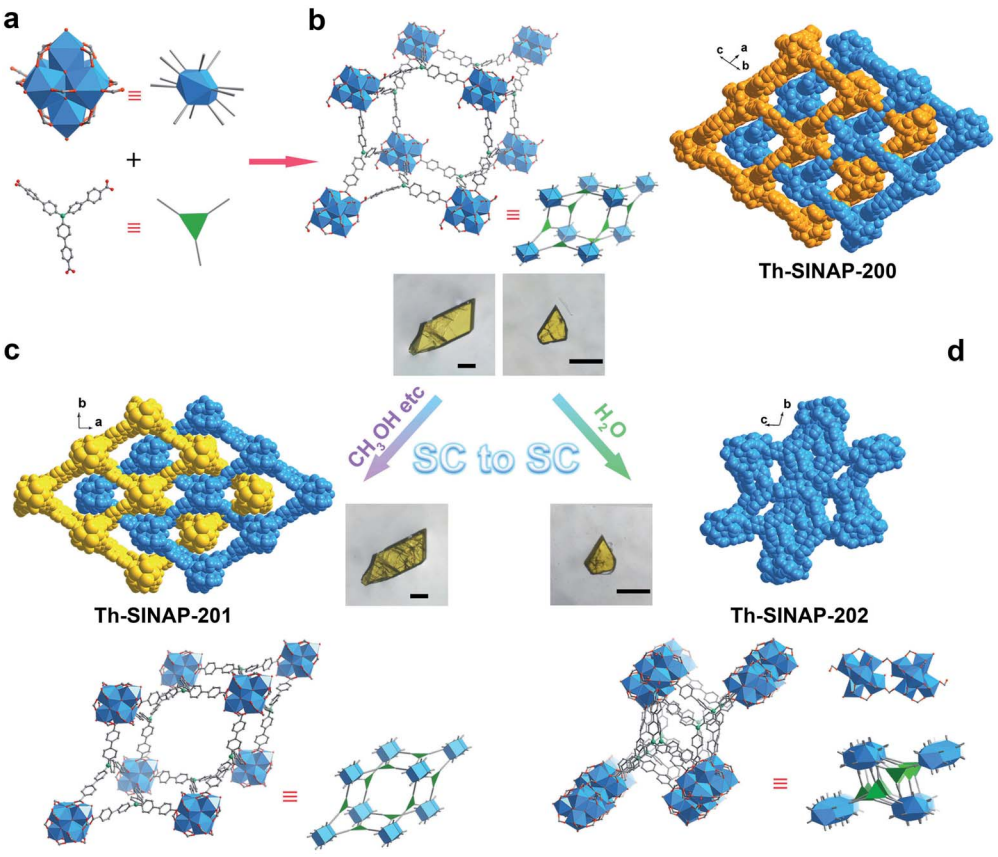

Fig. 1 (a) The 12-coordinated $Th_6(\mu_3\text{-}OH)_8(HCOO)_2(R\text{–}COO)_{12}$ cluster, triangular $TCBPA^{3-}$ ligand, simplified metal node, and simplified linker in **Th-SINAP-200**. (b) The 3D network, simplified topology, two-fold interpenetrated structure, and micrographs of **Th-SINAP-200**. Only O atoms of DMF molecules are shown for clarity. (c) The 3D network, simplified topology, two-fold interpenetrated structure, and micrograph of **Th-SINAP-201**. (d) The 3D network, simplified topology, and micrograph of **Th-SINAP-202**. Color code: Th polyhedra, light blue; C, gray; O, red; N, green. The scale bars in photographs represent 100 μm length.

© 2021 The Author(s). Published by the Royal Society of Chemistry

Open Access Article. Published on 20 October 2021. Downloaded on 5/3/2026 9:02:40 PM. This article is licensed under a Creative Commons Attribution-NonCommercial 3.0 Unported Licence.

Results and discussion

SC–SC transformation

Solvothermal reaction between $Th(NO_3)_4$ and tris(4′-carboxybiphenyl)amine (H_3TCBPA) in DMF in the presence of concentrated hydrochloric acid or formic acid as the modulator affords large (up to 400 μm) yellow block crystals of **Th-SINAP-200** with 36% yield. It is noteworthy that synthesizing the Zr and Hf analogues of **Th-SINAP-200** under similar synthetic conditions was attempted but unsuccessful. The only relevant Zr-MOF built from the same organic linker is Zr_{12}-NBC, which was obtained as fine powder and structurally characterized by powder X-ray diffraction (PXRD).[48] SCXRD analysis revealed that **Th-SINAP-200** crystallizes in the triclinic space group $P\bar{1}$. Owing to the cationic feature of **Th-SINAP-200** (discussed later), all eight O atoms on the Th_6 core were assigned as μ_3-OH groups, affording a $Th_6(\mu_3\text{-OH})_8$ hexameric SBU (Fig. 1a). Similar assignments to ensure the electroneutrality of Zr-MOFs have been demonstrated in NU-1000 and MOF-545.[49,50] Each SBU is further interconnected by twelve bridging $TCBPA^{3-}$ ligands, of which ten are coordinated in a bidentate mode and the remaining two are engaged in a monodentate manner (Fig. 2a). The affording moiety is further decorated by two $HCOO^-$ anions, three H_2O molecules, and one DMF molecule. Two crystallographically independent μ_3-η^2:η^2:η^1 tritopic $TCBPA^{3-}$ ligands and two unique μ_3-η^2:η^2:η^2 $TCBPA^{3-}$ linkers connect with Th_6 clusters *via* their carboxylate ends to form a 3D framework (Fig. 1b). Consequently, the Th_6 cluster and $TCBPA^{3-}$ can be interpreted as 12-connected SBU and 3-connected linkers, respectively. Two independent frameworks interpenetrate with each other, thus furnishing a 2-fold interpenetrated network, which can be simplified as a (3,12)-c net of *llj* topology with the point symbol $[4^{20}.6^{28}.8^{18}][4^3]4$. A large void space can be identified in **Th-SINAP-200** and its solvent accessible volume was calculated to be 53.1% based on *PLATON*.[51] Nitrates can be considered as anion species in the voids to maintain the charge balance of **Th-SINAP-200** as confirmed by its Fourier transform infrared (FTIR) spectrum, in which the characteristic peaks of NO_3^- were identified at 831 and 1386 cm^{-1} (Fig. S1†). Moreover, the cationic nature of **Th-SINAP-200** was evidenced by a competing cation/anion exchange study (Sr^{2+} *vs.* $Cr_2O_7^{2-}$), showing rapid uptake of $Cr_2O_7^{2-}$ by **Th-SINAP-200** and approximately unchanged concentration of Sr^{2+} in solution (Fig. S2†).

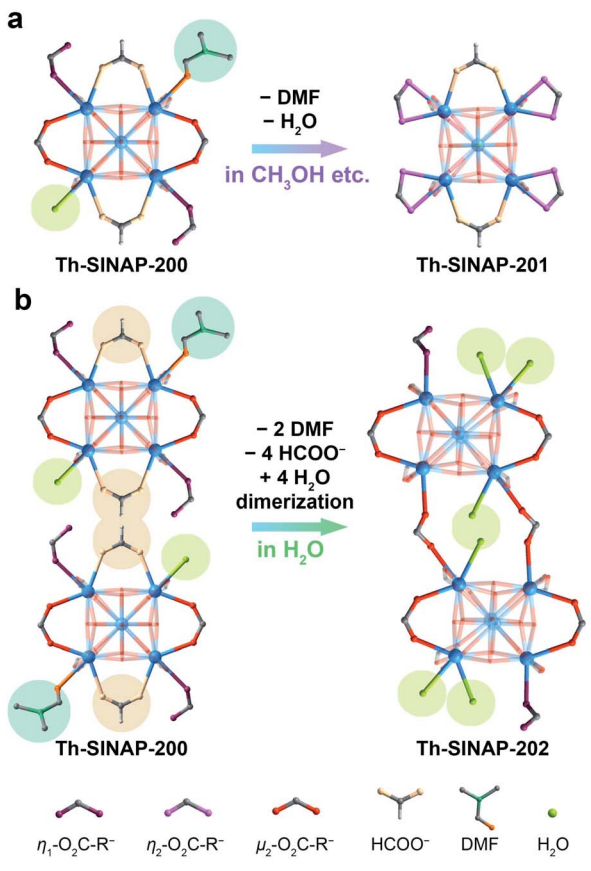

Fig. 2 Schematic diagrams showing the evolution of coordination environments of $Th_6(\mu_3\text{-OH})_8$ SBUs (a) from **Th-SINAP-200** to **Th-SINAP-201** and (b) from **Th-SINAP-200** to **Th-SINAP-202**. Only the coordination environments on the equatorial planes are shown and eight $TCBPA^{3-}$ ligands are omitted for clarity.

Notably, **Th-SINAP-200** exhibits fast SC–SC transformation to a new phase $[Th_6(\mu_3\text{-OH})_8(H_2O)_2(TCPBA)_4(HCOO)_2]\cdot(NO_3)_2$, namely **Th-SINAP-201**, upon immersion in a variety of organic solvents, including methanol, ethanol, acetonitrile, acetone, 1,4-dioxane, or *n*-hexane for 5 to 20 min at room temperature (Fig. 1c and S3†). A crystallographic study indicated that **Th-SINAP-201** crystallizes in the monoclinic space group *C*2/*m* with higher symmetry and features an identical *llj* topology compared with **Th-SINAP-200** (Table S1†). Correspondingly, a similar 3D structure and a comparable solvent-accessible volume (54.6%) were identified in **Th-SINAP-201** (Fig. 1c). However, bond cleavage and formation occurred between $Th_6(\mu_3\text{-OH})_8$ SBUs and $TCBPA^{3-}$ ligands/water molecules during SC–SC transformation. Explicitly, the $Th_6(\mu_3\text{-OH})_8$ SBU of **Th-SINAP-201** is coordinated with twelve $TCBPA^{3-}$ ligands exclusively in a bidentate fashion, with eight of them coordinating with two Th^{4+} cations and four of them chelating with one Th^{4+} cation of the Th_6 node (Fig. 2a). Moreover, departures of one H_2O and one DMF molecule on the equatorial plane of the Th_6 SBU in **Th-SINAP-200** occur due to the regeneration of four Th–η_2-O_2C–R bonds, while two $HCOO^-$ anions remain coordinated with the Th_6 SBU. Those SBUs are further interconnected by two crystallographically independent tritopic μ_3-η^2:η^2:η^2 $TCBPA^{3-}$ linkers to form a 2-fold interpenetrated framework.

More impressively, **Th-SINAP-200** transits into a distinct phase of $[Th_6(\mu_3\text{-OH})_8(H_2O)_5(TCPBA)_4]\cdot(NO_3)_4$ (**Th-SINAP-202**) when it is soaked in water for 30 min. The crystallinity of **Th-SINAP-202** is not as well maintained as that of **Th-SINAP-201**. Fortunately, the large and high-quality single crystal of its precursor makes elucidating the structure of **Th-SINAP-202** feasible (Fig. 1d). **Th-SINAP-202** crystallizes in monoclinic space group *C*2/*c* instead of *C*2/*m* in **Th-SINAP-201**, and its unit cell parameters and topology are completely changed (Table S1†). One of the most noteworthy variations is the conversion from a 2-fold interpenetrated framework in **Th-SINAP-200** to a non-

Open Access Article. Published on 20 October 2021. Downloaded on 5/3/2026 9:02:40 PM.
This article is licensed under a Creative Commons Attribution-NonCommercial 3.0 Unported Licence.

interpenetrated one in **Th-SINAP-202** (Fig. 1d). It is worth noting that this is the first example of interpenetration conversion of TOFs and it also represents the first case of SC–SC transformation of TOFs with topological changes. Consequently, **Th-SINAP-202** has a lower solvent-accessible volume than **Th-SINAP-200** (38.7% *versus* 53.1%) due to its denser packing manner. Two independent networks are interconnected into a new one *via* $[Th_6(\mu_3\text{-}OH)_8]$ dimerization, affording a $[Th_{12}(\mu_3\text{-}OH)_{16}]$ moiety *via* the bridging of two $TCBPA^{3-}$ ligands (Fig. 2b). This movement is further associated with the departure of two water molecules, two DMF molecules, and four formate groups, as well as the regeneration of six Th–O_w bonds. Therefore, reductions in coordination number from nine for **Th-SINAP-200** to eight for Th1 and Th6 cations in **Th-SINAP-202** were observed. The resultant $[Th_{12}(\mu_3\text{-}OH)_{16}(H_2O)_{10}]$ moiety is connecting to 24 neighboring ones *via* 24 $TCBPA^{3-}$ linkers, leading to a 24-connected porous framework, which can be described as a 3,3,24-c net with the point symbol $\{4^3\}8\{4^{64}.6^{140}.8^{72}\}$.

The spontaneous SC–SC transition of **Th-SINAP-200** to **Th-SINAP-201** in the aforementioned solvents makes precise measurement of the surface area of the former phase rather challenging, as activation of MOFs *via* solvent exchange is often required to remove guest species.[52] Therefore, N_2 adsorption/desorption analysis (77 K) on all TOFs was obtained by pretreating those materials under vacuum for 6 h at 200 °C. As shown in Fig. S4,† **Th-SINAP-200**, **Th-SINAP-201**, and **Th-SINAP-202** show typical type I isotherms, with Brunauer–Emmett–Teller (BET) areas calculated to be 415.4, 309.7, and 285.1 $m^2\ g^{-1}$, respectively. Thermogravimetric analysis (TGA) revealed that **Th-SINAP-200**, **Th-SINAP-201** (synthesized by immersing **Th-SINAP-200** in CH_3CN), and **Th-SINAP-202** are stable up to approximately 520 °C, approaching the record value (525 °C) of GWMOF-13 among all TOFs (Fig. S5†).[53] Moreover, **Th-SINAP-200** contains a much higher weight percentage (27%) of solvent species than those of **Th-SINAP-201** (17%) and **Th-SINAP-202** (11%). These differences can be attributed to the larger

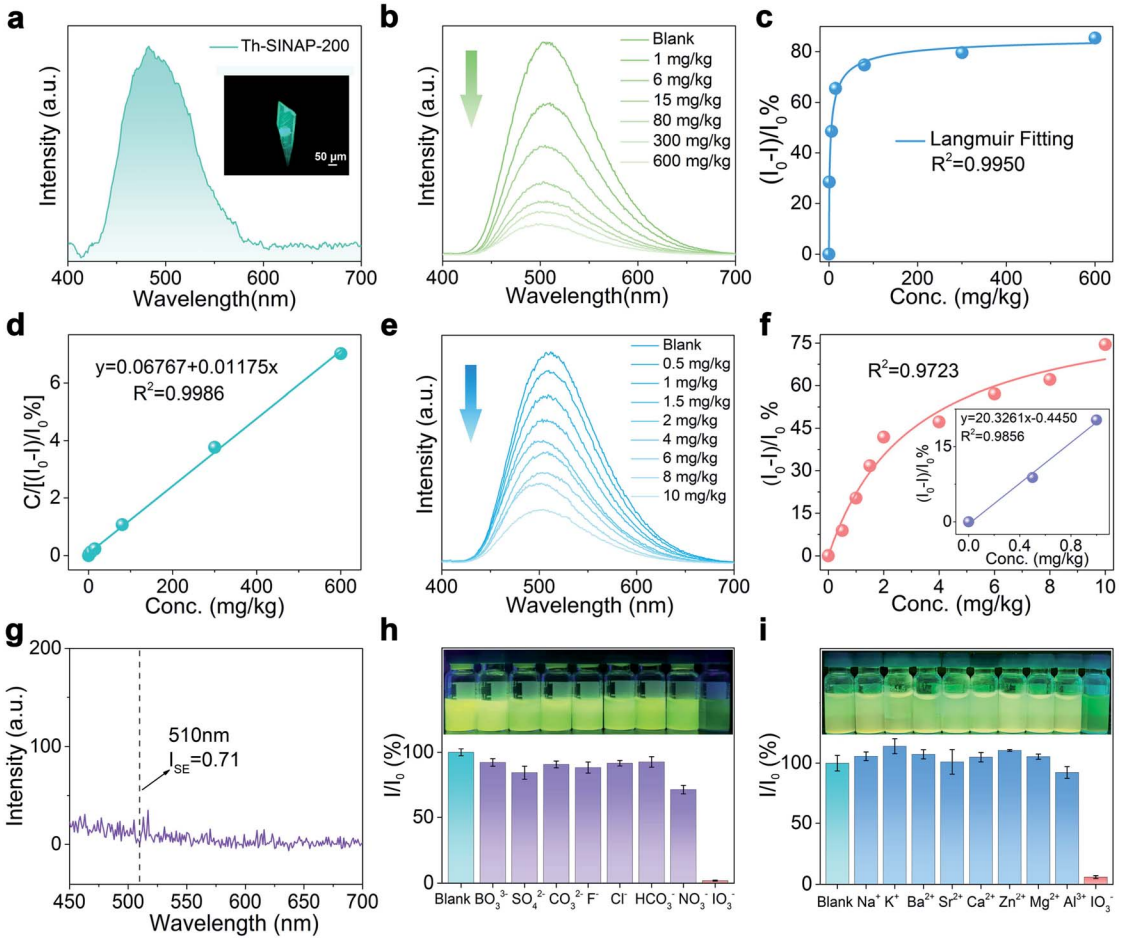

Fig. 3 (a) Solid-state PL spectrum (λ_{ex} = 365 nm) and optical micrograph of **Th-SINAP-200** under 365 nm UV excitation. (b) PL spectra of **Th-SINAP-200** titrated with different concentrations of IO_3^-. (c) Correlation between the quenching ratio $(I_0 - I)/I_0$ and IO_3^- concentration fitted with the Langmuir model. (d) Correlation between $C/[(I_0 - I)/I_0]$ and IO_3^- concentration. (e) PL spectra (λ_{ex} = 365 nm) of **Th-SINAP-200** titrated with concentrations of IO_3^- ranging from 0 to 10 mg kg^{-1}. (f) Correlation between the quenching ratio $(I_0 - I)/I_0$ and IO_3^- concentration at the low concentration range. Inset: linear fit of $(I_0 - I)/I_0$ as a function of IO_3^- concentration ranging from 0 to 1 mg kg^{-1}. (g) The standard error of PL intensity measurement determined from the baseline measurement of blank samples monitored at 510 nm. (h) Photographs and PL intensities of **Th-SINAP-200** immersed in different anion solutions. (i) Photographs and PL intensities of **Th-SINAP-200** immersed in different cation solutions.

© 2021 The Author(s). Published by the Royal Society of Chemistry

Open Access Article. Published on 20 October 2021. Downloaded on 5/3/2026 9:02:40 PM. This article is licensed under a Creative Commons Attribution-NonCommercial 3.0 Unported Licence.

molecular weight of DMF in **Th-SINAP-200** than CH_3CN in **Th-SINAP-201** and H_2O in **Th-SINAP-202**, further confirming that guest exchange is the driving force for the SC–SC transformations of **Th-SINAP-200**.

PL quenching for iodate sensing

Given the cationic nature and guest dependent SC–SC transformations of **Th-SINAP-200**, we speculated that interactions between the host framework and iodate may potentially trigger structural transformation accompanied by PL evolution.[54,55] To verify this hypothesis, the PL spectrum of **Th-SINAP-200** was collected as shown in Fig. 3a. A single crystal of **Th-SINAP-200** exhibits strong and visible green emission under 365 nm UV light excitation, corresponding to the broad PL band with λ_{max} at 482 nm. Such emission can be assigned to the π–π* or n–π* transition occurring within the $TCBPA^{3-}$ linker, as preliminarily ascertained by the similar excitation and emission spectra of H_3TCBPA (Fig. S6 and S7†).[56] Furthermore, the PL decay curves shown in Fig. S8† suggest comparable lifetimes (6.48 *vs.* 5.77 μs) of **Th-SINAP-200** and H_3TCBPA, confirming the ligand-based emission of **Th-SINAP-200**. Notably, the PL quantum yield of **Th-SINAP-200** was determined to be 26.64%, which is approximately one order of magnitude higher than that of the naked H_3TCBPA ligand (2.51%) (Fig. S9†).[57] This remarkable increase in quantum efficiency can be attributed to the ordered and spatial distribution of $TCBPA^{3-}$ ligands in the framework of **Th-SINAP-200**, which effectively eliminates luminescence quenching induced by agglomeration and nonradiative relaxation.[11,58–60]

Interestingly, the iodate concentration dependent luminescence study revealed a gradual decrease in the PL intensity of **Th-SINAP-200** at 510 nm with increasing IO_3^- concentrations (1 to 600 mg kg^{-1}, solid/liquid ratio = 1 g L^{-1}) (Fig. 3b). Correspondingly, the PL quenching ratio $(I_0 - I)/I_0$ increases with increasing IO_3^- concentrations and reaches 85.4% at 600 mg kg^{-1} (Fig. 3c). Simple mathematical transformation can establish a linear correlation ($R^2 = 0.9986$) between $C/[(I_0 - I)/I_0]$ and C, where C is the iodate concentration (Fig. 3d). Such a good linear relationship allows for accurate quantification of iodate over a broad concentration range from 1 to 600 mg kg^{-1}. Thanks to its high quantum efficiency, obvious PL variation of **Th-SINAP-200** can be observed in the presence of merely 0.5 mg kg^{-1} IO_3^- when the solid/liquid ratio decreases to 0.5 g L^{-1}. Further titration to 10 mg kg^{-1} IO_3^- results in a PL quenching ratio of 74.5%, indicating high detection sensitivity toward IO_3^- (Fig. 3e). To determine the LOD value, linear regression analysis was performed based on the equations LOD = 3σ/slope and $\sigma = 100 \times (I_{SE}/I_0)$, where I_{SE} is the standard error of the PL intensity measurement and I_0 is the PL intensity of **Th-SINAP-200** in deionized water (Fig. 3f and g). The LOD of IO_3^- for **Th-SINAP-200** was calculated to be 0.107 μg kg^{-1}, which is the lowest among those of all reported IO_3^- PL sensors and comparable to those based on spectrometric methods (Table S2†).[44–47]

To test the selective recognition of iodate and validate the real-world applicability of **Th-SINAP-200**, we evaluated the effects of a variety of cations and anions, which exist under environment related conditions, on the PL under parallel conditions. As illustrated in Fig. S10a,† **Th-SINAP-200** in different Na_xL ($L = IO_3^-$, BO_3^{3-}, SO_4^{2-}, CO_3^{2-}, F^-, Cl^-, HCO_3^-, or NO_3^-, $x = 1$, 2, or 3, 500 mg kg^{-1}) solutions exhibits a similar emission feature with a PL band centered at 510 nm. However, IO_3^- shows a much more effective quenching effect (91.8%) on the PL of **Th-SINAP-200**, than the remaining anions (10.0% to 41.3%) (Fig. 3h). The interference of Na^+ and other potential cations existing in the environment was further evaluated, showing negligible PL intensity reduction (Fig. 3i and S10b†). To accurately evaluate the detection sensitivity of **Th-SINAP-200** toward different anions, the Stern–Volmer equation ($I_0/I = K_{SV}[Q] + 1$, where I_0 and I are PL intensities before and after adding ions, respectively, and [Q] is the concentration of ions) was used to calculate the quenching constants (K_{SV}), showing that the K_{SV} of IO_3^- (2.2×10^4) is two to three orders of magnitude larger than those of the remaining ions (Table S3†).[61] These results demonstrate the excellent selectivity of **Th-SINAP-200** toward IO_3^- over the environmentally abundant cation and anion species.

PL quenching mechanism

Luminescence quenching can be explained by a variety of mechanisms, including inner filter effect, chemical conversion, resonance energy transfer, photoelectron transfer, structural transformation, and so forth.[62,63] To obtain mechanistic insight into that of **Th-SINAP-200**, the adsorption capacity toward IO_3^- was initially investigated by SEM-EDS, FTIR, and ICP-MS measurements. The elemental mapping analysis shown in Fig. S11† indicated that iodate was adsorbed and uniformly distributed on the crystalline material. FTIR analysis disclosed the occurrence of an anion exchange process, as evidenced by the emerging of ν_1 and ν_3 I–O stretching bands (782 and 725 cm^{-1}) and concurrently reduced intensity of ν_1 N–O stretching bands (1091 cm^{-1}) (Fig. S1†).[64] A sorption kinetic study further revealed that fast adsorption equilibrium (within 30 min) can be achieved for IO_3^-, which is in accordance with its prompt PL quenching

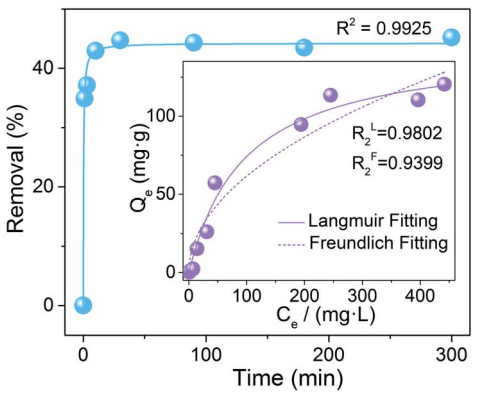

Fig. 4 Removal percentage of IO_3^- as a function of contact time fitted with the pseudo-second-order kinetic model. Inset: adsorption isotherms of IO_3^- by Th-SINAP-200 fitted with the Langmuir model and the Freundlich model.

Open Access Article. Published on 20 October 2021. Downloaded on 5/3/2026 9:02:40 PM. This article is licensed under a Creative Commons Attribution-NonCommercial 3.0 Unported Licence.

response upon coming into contact with IO_3^- (Fig. 4). The sorption kinetics of IO_3^- toward **Th-SINAP-200** can be well fitted by the pseudo-second-order kinetic model with a correlation coefficient value (R^2) of 0.9912, suggesting the rate controlling role of chemisorption (Table S4†). Furthermore, the adsorption isotherm can be well fitted with a Langmuir model ($R^2 = 0.9803$), showing a maximum adsorption capacity of 152.6 mg g^{-1} (Fig. 4 inset and Table S5†). Such a correlation is in line with the PL quenching behavior of **Th-SINAP-200**, which also obeys the Langmuir model with an R^2 of 0.9884 (Fig. 3e). These results conjointly suggest a sorption based quenching mechanism for **Th-SINAP-200**.

More gratifyingly, both the morphology and crystallinity of **Th-SINAP-200** can be preserved after anion exchange with iodate in 600 mg kg^{-1} $NaIO_3$ solution (Fig. 5a). The SCXRD study revealed that **Th-SINAP-200** suffers from a distinct structural evolution, implying a SC–SC transformation-based PL quenching mechanism. The new phase, namely **Th-SINAP-203**, crystallizes in the same space group of $P\bar{1}$ but with different unit cell parameters compared to **Th-SINAP-200**. No significant variations of overall topology and pore volume (50.4%) were observed (Fig. 5b and Table S1†). However, the conformations of $TCBPA^{3-}$ linkers undergo dramatic changes as defined by the torsion angle of two neighboring phenyl groups. Explicitly, the largest torsion angle of the ligands in **Th-SINAP-203** increases up to 47.09°, compared to 39.52° in **Th-SINAP-200** (Fig. 5c and Table S6†). This conformation change will necessarily result in a higher degree of excited-state distortion, which ultimately contributes to the quenching of ligand-based emission.[11] Another noteworthy feature is the change of coordination environments of SBUs, which undergo the departure of two $HCOO^-$ anions and one DMF molecule, and incorporation of a water molecule (Fig. 5d). One may note that Th2, Th4, Th8, and Th10 in **Th-SINAP-203** are eight coordinated, contrasting sharply with the dominance of nine-coordinated Th cations in **Th-SINAP-200** and **Th-SINAP-201**. Such reductions in coordination number give rise to open metal sites for iodate sorption. Modeling IO_3^- anions within **Th-SINAP-203** was attempted but unsuccessful due to the absence of localized electron densities suitable for IO_3^- assignment. One possible explanation is that the adsorbed IO_3^- anions could be highly disordered, which is frequently observed in host–guest systems.[65,66]

To elucidate the host–guest interaction between the framework of **Th-SINAP-203** and iodate, we further conducted an X-ray absorption near-edge spectroscopy (XANES) study on iodate adsorbed **Th-SINAP-203**. The XANES spectrum shows a pre-edge peak at 4562 eV, corresponding to the 2p → 5d transition of iodate (Fig. 5e).[67] Furthermore, its overall profile is

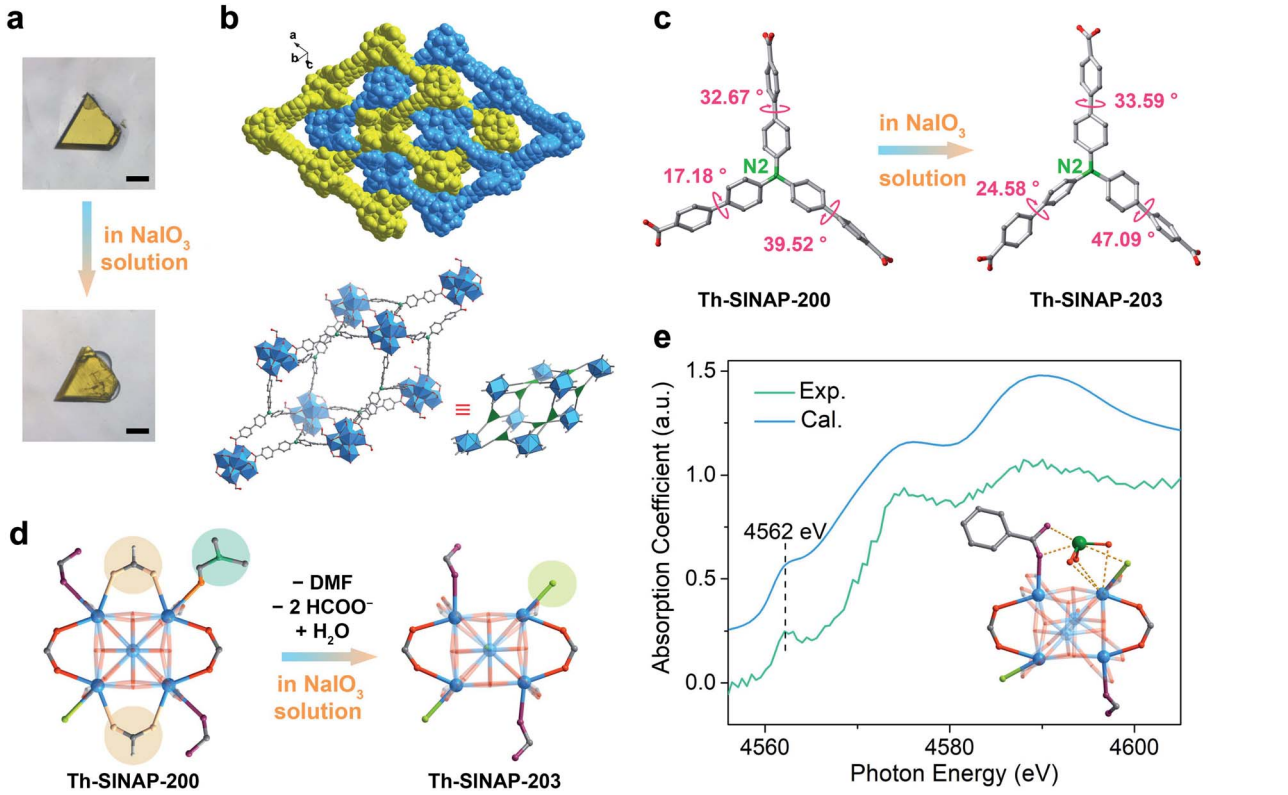

Fig. 5 (a) Micrographs showing the SC–SC transformation from **Th-SINAP-200** to **Th-SINAP-203**. The scale bar in the photograph represents 100 μm length. (b) The 3D network, simplified topology, two-fold interpenetrated structure, and micrograph of the transformed **Th-SINAP-203**. (c) The change of ligand conformations from **Th-SINAP-200** to **Th-SINAP-203**. (d) Schematic diagrams showing the evolution of coordination environments of $Th_6(\mu_3\text{-}OH)_8$ SBUs from **Th-SINAP-200** to **Th-SINAP-203**. Only coordination environments on the equatorial planes are shown and eight $TCBPA^{3-}$ ligands are omitted for clarity. (e) Experimental and simulated XANES spectra of **Th-SINAP-203**. Inset: the modeled coordination environment of IO_3^- (color code: I in green).

© 2021 The Author(s). Published by the Royal Society of Chemistry

Open Access Article. Published on 20 October 2021. Downloaded on 5/3/2026 9:02:40 PM.
This article is licensed under a Creative Commons Attribution-NonCommercial 3.0 Unported Licence.

slightly different from that of the free IO_3^- anion in an aqueous solution, revealing interactions existing between the framework and iodate.[68] Moreover, modeling the IO_3^- anion at the second coordination sphere of Th1 with open metal sites successfully gives rise to a simulated XANES profile comparable with the experimental one. The Th–O_{iodate} distance was calculated to be approximately 3.035 Å, indicating moderate interaction between the framework and IO_3^-, and hence, a static quenching mechanism. Specifically, the spin–orbit coupling of the excited $TCBPA^{3-}$ ligand and heavy IO_3^- anion results in an efficient intersystem crossing (ISC) process from the singlet (S_1) to the triplet state (T_1), which is nonradiative and causes PL quenching (Fig. S12†).[61] The long-lived triplet excited state (T_1) can be further quenched to the ground state (S_0) *via* a nonradiative decay pathway or by the same IO_3^- quencher.

In brief, the sensitive and selective sensing capability of **Th-SINAP-200** toward iodate can be attributed to the following reasons. First, the SC–SC transition induced by iodate sorption leads to large modifications of the $TCBPA^{3-}$ conformation, giving rise to PL quenching in a structural transformation mechanism. Second, the host–guest interaction between the luminescent framework and iodates results in heavy atom induced intersystem crossing, leading to a selective and static quenching by a distinct mechanism.

Conclusions

In summary, we have demonstrated a cationic TOF, **Th-SINAP-200**, showing unprecedented triple SC–SC transformations with both its topology and degree of interpenetration being modified. One key feature of **Th-SINAP-200** is the appropriate hardness of Th^{4+} cations, which predisposes the TOF to crystallize into large and high-quality single crystals suitable for elucidating its own structure and any transformed phases. In contrast, attempts to isolate the single crystals of Zr and Hf analogues were unsuccessful. Therefore, the full extent of the structural transformations of this TOF can be visualized by SCXRD, from **Th-SINAP-200** to **Th-SINAP-201**, **Th-SINAP-202**, and **Th-SINAP-203**, respectively, in a variety of organic solvents, water, and $NaIO_3$ solution. Notably, both the SC–SC transformation with a topological change and interpenetration conversion occurring in **Th-SINAP-202** are unprecedented for TOFs. Furthermore, the coordination environment of SBUs undergoes dramatic changes in **Th-SINAP-203**, despite the fact that its overall topology is well inherited from **Th-SINAP-200**. The ultimate outcome of such variations combined with the conformation change of $TCBPA^{3-}$ linkers in **Th-SINAP-203** leads to the efficient turn-off of the ligand-based emission in **Th-SINAP-200**, giving rise to an extremely low LOD (0.107 μg kg^{-1}) toward iodate. To the best of our knowledge, this value is the lowest among those of all known iodate PL sensors and comparable to those based on spectrometric methods. This work clearly shows that TOFs represent a unique and promising platform for engineering materials with SC–SC transformation features to probe mechanistic features pertaining to ion exchange, chemosensing, *etc.*

Experimental

Materials

Caution! Th-232 and its daughter nucleus Ra-228 are both radioactive. All of the thorium compounds used and investigated were operated in an authorized laboratory designed for actinide element studies. Standard precautions for radioactive materials should be followed.

All reagents were purchased from chemical reagent suppliers and used without further purification. *N*,*N*′-Dimethylformamide (DMF, 99%), formic acid (98%+), *n*-hexane (97%, SafeDry), 1,4-dioxane (99%+), $NaIO_3$ (99%), $AlCl_3$ (99.99%), Na_2CO_3 (99.95%), and $NaHCO_3$ (99%, Adamas) were provided by Adamas. Na_2SO_4 (≥99.0%), NaF (99%), NaCl (≥99.5%), MeOH (≥99.5%), and acetonitrile (CH_3CN, ≥99.0%) were from Greagent. Concentrated hydrochloric acid (36.0–38.0%), ethanol (≥99.7%), acetone (99.5%), ethyl ether (99%), NaCl (99%), KCl (99%), $BaCl_2$ (99%), $SrCl_2$ (99%), $CaCl_2$ (99%), $ZnCl_2$ (99%), $MgCl_2$ (99%), and Na_3BO_3 (99%) were provided by Sinopharm Chemical Reagent Co., Ltd. Other reagents: $Th(NO_3)_4 \cdot 6H_2O$ (99%, Changchun Institute of Applied Chemistry, CAS) and tris((4-carboxyl)phenylduryl)amine (98%, Jilin Chinese Academy of Sciences – Yanshen Technology Co., Ltd.).

Synthesis

Th-SINAP-200. $Th(NO_3)_4 \cdot 6H_2O$ (4.7 mg, 0.008 mmol), tris(4′-carboxybiphenyl)amine (H_3TCBPA, 2.4 mg, 0.004 mmol), DMF (0.37 mL), and formic acid (0.04 mL) or concentrated hydrochloric acid (0.08 mL) were loaded in a capped vial and heated at 120 °C for 24 h. Yellow block crystals of **Th-SINAP-200** were filtered, washed with DMF several times, and dried at room temperature for several days. The yield was calculated to be 36% based on H_3TCBPA. Anal. calcd for $C_{209}H_{277}N_{23}Th_6O_{85}$, C, 42.81%; H, 4.76%; N, 5.49%. Found: C, 43.17%; H, 5.12%; N, 5.15%. IR: 3034 (w), 3034 (w), 2854 (w), 2034 (w), 1704 (w), 1652 (vs), 1593 (vs), 1540 (w), 1521 (m), 1490 (m), 1386 (s), 1322 (w), 1278 (w), 1254 (w), 1189 (m), 1090 (s), 1061 (w), 1017 (w), 1005 (w), 867 (w), 831 (s), 783 (s), 747 (w), 726 (m), 705 (w), 656 (w), 577 (w), 549 (w), 528 (w).

Th-SINAP-201. The yellow crystals of **Th-SINAP-201** were obtained through immersing **Th-SINAP-200** in CH_3CN for 1 hour. Yellow crystals were filtered, washed with CH_3CN, and dried at room temperature. Anal. calcd for $C_{184}H_{187}N_{19}Th_6O_{63}$, C, 43.63%; H, 3.72%; N, 5.25%. Found: C, 43.86%; H, 3.57%; N, 5.14%. IR: 3031 (w), 2250 (w), 1702 (w), 1657 (w), 1590 (vs), 1538 (w), 1519 (v), 1490 (m), 1398 (vs), 1323 (w), 1280 (w), 1190 (m), 1104 (s), 1017 (w), 1004 (w), 919 (w), 832 (m), 783 (s), 748 (w), 726 (m), 705 (w), 652 (w), 575 (w), 530 (w).

Th-SINAP-202. The crystals of **Th-SINAP-202** were obtained through immersing **Th-SINAP-200** in H_2O for 2 h. Yellow crystals were filtered, washed with H_2O, and dried at room temperature. Anal. calcd for $C_{315}H_{323}N_{17}Th_{12}O_{143}$, C, 40.17%; H, 3.46%; N, 2.53%. Found: C, 40.42%; H, 3.34%; N, 2.34%. IR: 3031 (w), 1670 (w), 1652 (w), 1589 (s), 1519 (v), 1489 (m), 1397 (vs), 1321 (w), 1278 (w), 1188 (w), 1104 (w), 1015 (w), 1004 (w), 864 (w), 827 (w), 782 (s), 748 (w), 725 (w), 704 (w), 650 (w), 638 (w).

Open Access Article. Published on 20 October 2021. Downloaded on 5/3/2026 9:02:40 PM. This article is licensed under a Creative Commons Attribution-NonCommercial 3.0 Unported Licence.

Crystallographic studies

SCXRD data of the four TOFs were collected on a Bruker D8-Venture single-crystal X-ray diffractometer equipped with a Turbo X-ray source (Mo Kα radiation, $\lambda = 0.71073$ Å) adopting the direct-drive rotating-anode technique and a CMOS detector at 120 K. The data frames were collected using the APEX3 program and processed using the SAINT routine. The empirical absorption correction was conducted using the SADABS program.[69] The structure was solved by Intrinsic Phasing with *ShelXT*[70] and refined with a full-matrix least-squares technique of ShelXL[71] interpreted by Olex2.[72] Anisotropic thermal parameters were applied to all nonhydrogen atoms. The hydrogen atoms were generated by the riding mode. For **Th-SINAP-200**, several benzene rings were two-fold disordered and modeled with PART command. DFIX, SADI, SIMU, RIGU, FLAT, ISOR, and EADP restraints were used to obtain reasonable parameters due to the poor quality of crystal data for **Th-SINAP-202** and **Th-SINAP-203**. The large R indices of **Th-SINAP-202** and **Th-SINAP-203** can be attributed to the decreased quality of the single crystals after SC–SC transitions, giving rise to poor diffraction data with low resolutions of 1.25 Å and 1.1 Å, respectively. All the counter ions and solvent molecules of the four TOFs are highly disordered and cannot be modeled for refinement. Contributions to the scattering from these species were removed using the *SQUEEZE* routine of *PLATON*.[73] Structures were then refined again using the data generated. Crystal data and details of the data collection are given in Table S1.†

Characterization

PXRD data were collected from 2 to 40° with a step of 0.02° on a Bruker D8 Advance diffractometer with Cu Kα radiation ($\lambda =$ 1.54178 Å). The calculated PXRD pattern was produced from the CIFs using the Mercury 1.4.2 program. The N_2 adsorption isotherms were recorded at 77 K by using a Micromeritics ASAP 2020. The freshly prepared TOFs were directly evacuated under vacuum for 6 h at 200 °C before measurement. Thermogravimetric analysis (TGA) was carried out in a N_2 atmosphere with a heating rate of 10 °C min^{-1} on a NETZSCH STA 449 F3 Jupiter instrument. SEM images and EDS data were obtained on a Zeiss Merlin Compact LEO 1530 VP scanning electron microscope. The IR spectra with a range of 400 to 4000 cm^{-1} were recorded on a Thermo Nicolet 6700 FTIR spectrometer equipped with a diamond attenuated total reflectance (ATR) accessory. The solid-state PL spectrum of **Th-SINAP-200** was recorded on a Craic Technologies microspectrophotometer. The excitation and emission spectra, decay curves, and PL quantum-yields were collected on an Edinburgh Instruments FLS 980 spectrofluorometer.

X-ray absorption near edge spectroscopy study

The XANES data at the I L_3 edge were collected on beamline 14W1 at the Shanghai Synchrotron Radiation Facility (SSRF).[74] The electron beam energy was 3.5 GeV with a stored current of approximately 230 mA in top-up operation. A fixed-exit double crystal Si ⟨111⟩ monochromator was applied for the incident energy selection. The XANES spectra were collected in fluorescence mode employing a 7-element Ge solid state detector. The analysis of the I L_3-edge XANES data was carried out with standard procedures by utilizing the software package of Demeter.[75] The *ab initio* multiple scattering theory based code FEFF 9.6 was applied for the calculation of the I L_3-edge XANES spectra of the sample.[76] The input file contained coordinates of neighboring atoms within a single-scattering path length of 15.0 Å. The atomic potentials were calculated self consistently on a cluster with a radius of 4.0 Å and about 15 atoms in the presence of a core-hole. The exchange–correlation Hedin–Lundquist potential was used. Full multiple scattering calculations were done on a cluster with a radius of 5.0 Å containing about 25 atoms.

Author contributions

J. L. conceived and designed the research. Z. J. L. and Y. J. synthesized the materials. Z. J. L. and Y. L. solved the crystal structures. M. L. and W. L. performed the PL study. Z. H. Z. performed the BET study. H. B. and X. G. conducted the XANES study and analyzed the data. J. L., J. Q. W., M. Y. H., W. L., Y. Q., and Z. J. L. analyzed the data and wrote the manuscript. All authors have given approval to the manuscript.

Conflicts of interest

The authors declare no competing financial interests.

Acknowledgements

We cordially thank Prof. Ning Chen (Chemical Engineering and Materials Science, Soochow University) for helpful discussions. We thank the members of the beamline BL14W1 at SSRF for the XANES study. This work was supported by the National Natural Science Foundation of China (22076196, 21906163, and 21876182), the Young Taishan Scholars Program (tsqn201909082), Natural Science Foundation of Shandong Province (ZR201910290031), the Strategic Priority Research Program of the Chinese Academy of Sciences (XDA21000000), and the K. C.Wong Education Foundation (GJTD-2018-10).

Notes and references

1 J. Pang, S. Yuan, J. Qin, M. Wu, C. T. Lollar, J. Li, N. Huang, B. Li, P. Zhang and H.-C. Zhou, *J. Am. Chem. Soc.*, 2018, **140**, 12328.
2 Y. Chen, X. Zhang, M. R. Mian, F. A. Son, K. Zhang, R. Cao, Z. Chen, S.-J. Lee, K. B. Idrees, T. A. Goetjen, J. Lyu, P. Li, Q. Xia, Z. Li, J. T. Hupp, T. Islamoglu, A. Napolitano, G. W. Peterson and O. K. Farha, *J. Am. Chem. Soc.*, 2020, **142**, 21428.
3 S. Yuan, J.-S. Qin, J. Su, B. Li, J. Li, W. Chen, H. F. Drake, P. Zhang, D. Yuan, J. Zuo and H.-C. Zhou, *Angew. Chem., Int. Ed.*, 2018, **57**, 12578.
4 L. Protesescu, J. Calbo, K. Williams, W. Tisdale, A. Walsh and M. Dincă, *Chem. Sci.*, 2021, **12**, 6129.

© 2021 The Author(s). Published by the Royal Society of Chemistry

Open Access Article. Published on 20 October 2021. Downloaded on 5/3/2026 9:02:40 PM.
This article is licensed under a Creative Commons Attribution-NonCommercial 3.0 Unported Licence.

5 J.-H. Dou, M. Q. Arguilla, Y. Luo, J. Li, W. Zhang, L. Sun, J. L. Mancuso, L. Yang, T. Chen, L. R. Parent, G. Skorupskii, N. J. Libretto, C. Sun, M. C. Yang, P. V. Dip, E. J. Brignole, J. T. Miller, J. Kong, C. H. Hendon, J. Sun and M. Dincă, *Nat. Mater.*, 2021, **20**, 222.

6 M. I. Gonzalez, A. B. Turkiewicz, L. E. Darago, J. Oktawiec, K. Bustillo, F. Grandjean, G. J. Long and J. R. Long, *Nature*, 2019, **577**, 64.

7 J. Albalad, H. Xu, F. Gándara, M. Haouas, C. Martineau-Corcos, R. Mas-Ballesté, S. A. Barnett, J. Juanhuix, I. Imaz and D. Maspoch, *J. Am. Chem. Soc.*, 2018, **140**, 2028.

8 M. Mon, J. Ferrando-Soria, M. Verdaguer, C. Train, C. Paillard, B. Dkhil, C. Versace, R. Bruno, D. Armentano and E. Pardo, *J. Am. Chem. Soc.*, 2017, **139**, 8098.

9 J. Baek, B. Rungtaweevoranit, X. Pei, M. Park, S. C. Fakra, Y.-S. Liu, R. Matheu, S. A. Alshmimri, S. Alshehri, C. A. Trickett, G. A. Somorjai and O. M. Yaghi, *J. Am. Chem. Soc.*, 2018, **140**, 18208.

10 H. Wang, Z. Shi, J. Yang, T. Sun, B. Rungtaweevoranit, H. Lyu, Y.-B. Zhang and O. M. Yaghi, *Angew. Chem., Int. Ed.*, 2021, **60**, 3417.

11 Z. Wei, Z.-Y. Gu, R. K. Arvapally, Y.-P. Chen, R. N. McDougald, J. F. Ivy, A. A. Yakovenko, D. Feng, M. A. Omary and H.-C. Zhou, *J. Am. Chem. Soc.*, 2014, **136**, 8269.

12 J. Zhang, L. Chen, X. Dai, L. Zhu, C. Xiao, L. Xu, Z. Zhang, E. V. Alekseev, Y. Wang, C. Zhang, H. Zhang, Y. Wang, J. Diwu, Z. Chai and S. Wang, *Chem*, 2019, **5**, 977.

13 L. Mei, F.-Z. Li, J.-H. Lan, C.-Z. Wang, C. Xu, H. Deng, Q.-Y. Wu, K.-Q. Hu, L. Wang, Z.-F. Chai, J. Chen, J. K. Gibson and W.-Q. Shi, *Nat. Commun.*, 2019, **10**, 1532.

14 K.-Q. Hu, P.-X. Qiu, L.-W. Zeng, S.-X. Hu, L. Mei, S.-W. An, Z.-W. Huang, X.-H. Kong, J.-H. Lan, J.-P. Yu, Z.-H. Zhang, Z.-F. Xu, J. K. Gibson, Z.-F. Chai, Y.-F. Bu and W.-Q. Shi, *Angew. Chem., Int. Ed.*, 2020, **59**, 20666.

15 X.-N. Wang, P. Zhang, A. Kirchon, J. Li, W.-M. Chen, Y.-M. Zhao, B. Li and H.-C. Zhou, *J. Am. Chem. Soc.*, 2019, **141**, 13654.

16 W. Gong, W. Zhang, F. A. Son, K. Yang, Z. Chen, X. Chen, J. Jiang, Y. Liu, O. K. Farha and Y. Cui, *Chem*, 2020, **7**, 190.

17 X. Zhang, B. L. Frey, Y.-S. Chen and J. Zhang, *J. Am. Chem. Soc.*, 2018, **140**, 7710.

18 S. Yuan, P. Zhang, L. Zhang, A. T. Garcia-Esparza, D. Sokaras, J.-S. Qin, L. Feng, G. S. Day, W. Chen, H. F. Drake, P. Elumalai, S. T. Madrahimov, D. Sun and H.-C. Zhou, *J. Am. Chem. Soc.*, 2018, **140**, 10814.

19 S. Yuan, Y.-P. Chen, J.-S. Qin, W. Lu, L. Zou, Q. Zhang, X. Wang, X. Sun and H.-C. Zhou, *J. Am. Chem. Soc.*, 2016, **138**, 8912.

20 Y. Wen, P. Zhang, V. K. Sharma, X. Ma and H.-C. Zhou, *Cell Rep. Phys. Sci.*, 2021, **2**, 100348.

21 C.-X. Chen, Z. Wei, J.-J. Jiang, Y.-Z. Fan, S.-P. Zheng, C.-C. Cao, Y.-H. Li, D. Fenske and C.-Y. Su, *Angew. Chem., Int. Ed.*, 2016, **55**, 9932.

22 R. Shannon, *Acta Crystallogr., Sect. A: Found. Crystallogr.*, 1976, **32**, 751.

23 Z.-J. Li, Y. Ju, B. Yu, X. Wu, H. Lu, Y. Li, J. Zhou, X. Guo, Z.-H. Zhang, J. Lin, J.-Q. Wang and S. Wang, *Chem. Commun.*, 2020, **56**, 6715.

24 Z.-J. Li, Y. Ju, H. Lu, X. Wu, X. Yu, Y. Li, X. Wu, Z.-H. Zhang, J. Lin, Y. Qian, M.-Y. He and J.-Q. Wang, *Chem.–Eur. J.*, 2021, **27**, 1286.

25 S. E. Gilson, M. Fairley, P. Julien, A. G. Oliver, S. L. Hanna, G. Arntz, O. K. Farha, J. A. LaVerne and P. C. Burns, *J. Am. Chem. Soc.*, 2020, **142**, 13299.

26 S. Krause, V. Bon, U. Stoeck, I. Senkovska, D. M. Többens, D. Wallacher and S. Kaskel, *Angew. Chem., Int. Ed.*, 2017, **56**, 10676.

27 Y. Zhang, X. Zhang, J. Lyu, K.-i. Otake, X. Wang, L. R. Redfern, C. D. Malliakas, Z. Li, T. Islamoglu, B. Wang and O. K. Farha, *J. Am. Chem. Soc.*, 2018, **140**, 11179.

28 B. Karadeniz, D. Žilić, I. Huskić, L. S. Germann, A. M. Fidelli, S. Muratović, I. Lončarić, M. Etter, R. E. Dinnebier, D. Barišić, N. Cindro, T. Islamoglu, O. K. Farha, T. Friščić and K. Užarević, *J. Am. Chem. Soc.*, 2019, **141**, 19214.

29 J. Lyu, X. Gong, S.-J. Lee, K. Gnanasekaran, X. Zhang, M. C. Wasson, X. Wang, P. Bai, X. Guo, N. C. Gianneschi and O. K. Farha, *J. Am. Chem. Soc.*, 2020, **142**, 4609.

30 Y. Wang, W. Liu, Z. Bai, T. Zheng, M. A. Silver, Y. Li, Y. Wang, X. Wang, J. Diwu, Z. Chai and S. Wang, *Angew. Chem., Int. Ed.*, 2018, **57**, 5783.

31 J.-Y. Kim, A. J. Norquist and D. O'Hare, *J. Am. Chem. Soc.*, 2003, **125**, 12688.

32 Z.-W. Huang, K.-Q. Hu, L. Mei, X.-H. Kong, J.-P. Yu, K. Liu, L.-W. Zeng, Z.-F. Chai and W.-Q. Shi, *Dalton Trans.*, 2020, **49**, 983.

33 Z. Xu, X. Xiong, J. Xiong, R. Krishna, L. Li, Y. Fan, F. Luo and B. Chen, *Nat. Commun.*, 2020, **11**, 3163.

34 P. Li, X. Wang, K.-i. Otake, J. Lyu, S. L. Hanna, T. Islamoglu and O. K. Farha, *ACS Appl. Nano Mater.*, 2019, **2**, 2260.

35 E. A. Dolgopolova, O. A. Ejegbavwo, C. R. Martin, M. D. Smith, W. Setyawan, S. G. Karakalos, C. H. Henager, H.-C. zur Loye and N. B. Shustova, *J. Am. Chem. Soc.*, 2017, **139**, 16852.

36 O. A. Ejegbavwo, C. R. Martin, O. A. Olorunfemi, G. A. Leith, R. T. Ly, A. M. Rice, E. A. Dolgopolova, M. D. Smith, S. G. Karakalos, N. Birkner, B. A. Powell, S. Pandey, R. J. Koch, S. T. Misture, H.-C. z. Loye, S. R. Phillpot, K. S. Brinkman and N. B. Shustova, *J. Am. Chem. Soc.*, 2019, **141**, 11628.

37 H. Xu, C.-S. Cao, H.-S. Hu, S.-B. Wang, J.-C. Liu, P. Cheng, N. Kaltsoyannis, J. Li and B. Zhao, *Angew. Chem., Int. Ed.*, 2019, **58**, 6022.

38 Y. Li, Z. Yang, Y. Wang, Z. Bai, T. Zheng, X. Dai, S. Liu, D. Gui, W. Liu, M. Chen, L. Chen, J. Diwu, L. Zhu, R. Zhou, Z. Chai, T. E. Albrecht-Schmitt and S. Wang, *Nat. Commun.*, 2017, **8**, 1354.

39 B. Manna, A. K. Chaudhari, B. Joarder, A. Karmakar and S. K. Ghosh, *Angew. Chem., Int. Ed.*, 2013, **52**, 998.

40 Y. Cui, Y. Yue, G. Qian and B. Chen, *Chem. Rev.*, 2012, **112**, 1126.

41 D. I. Kaplan, M. E. Denham, S. Zhang, C. Yeager, C. Xu, K. A. Schwehr, H. P. Li, Y. F. Ho, D. Wellman and

Open Access Article. Published on 20 October 2021. Downloaded on 5/3/2026 9:02:40 PM.
This article is licensed under a Creative Commons Attribution-NonCommercial 3.0 Unported Licence.

P. H. Santschi, *Crit. Rev. Environ. Sci. Technol.*, 2014, **44**, 2287.
42 S. Zhang, J. Du, C. Xu, K. A. Schwehr, Y. F. Ho, H. P. Li, K. A. Roberts, D. I. Kaplan, R. Brinkmeyer, C. M. Yeager, H.-s. Chang and P. H. Santschi, *Environ. Sci. Technol.*, 2011, **45**, 5543.
43 S. Zhang, C. Xu, D. Creeley, Y.-F. Ho, H.-P. Li, R. Grandbois, K. A. Schwehr, D. I. Kaplan, C. M. Yeager, D. Wellman and P. H. Santschi, *Environ. Sci. Technol.*, 2013, **47**, 9635.
44 K. Reddy-Noone, A. Jain and K. K. Verma, *J. Chromatogr. A*, 2007, **1148**, 145.
45 X. Huang, Y. Li, Y. Chen and L. Wang, *Sens. Actuators, B*, 2008, **134**, 780.
46 Y. C. Li, W. F. Bu, L. X. Wu and C. Q. Sun, *Sens. Actuators, B*, 2005, **107**, 921.
47 A. Salimi, A. Noorbakhsh and M. Ghadermarzi, *Sens. Actuators, B*, 2007, **123**, 530.
48 X.-N. Zou, D. Zhang, T.-X. Luan, Q. Li, L. Li, P.-Z. Li and Y. Zhao, *ACS Appl. Mater. Interfaces*, 2021, **13**, 20137.
49 W. Morris, B. Volosskiy, S. Demir, F. Gándara, P. L. McGrier, H. Furukawa, D. Cascio, J. F. Stoddart and O. M. Yaghi, *Inorg. Chem.*, 2012, **51**, 6443.
50 J. E. Mondloch, W. Bury, D. Fairen-Jimenez, S. Kwon, E. J. DeMarco, M. H. Weston, A. A. Sarjeant, S. T. Nguyen, P. C. Stair, R. Q. Snurr, O. K. Farha and J. T. Hupp, *J. Am. Chem. Soc.*, 2013, **135**, 10294.
51 A. Spek, *Acta Crystallogr., Sect. C: Struct. Chem.*, 2015, **71**, 9.
52 J. Ma, A. P. Kalenak, A. G. Wong-Foy and A. J. Matzger, *Angew. Chem., Int. Ed.*, 2017, **56**, 14618.
53 K. P. Carter, J. A. Ridenour, M. Kalaj and C. L. Cahill, *Chem.–Eur. J.*, 2019, **25**, 7114.
54 H. Fei, M. R. Bresler and S. R. J. Oliver, *J. Am. Chem. Soc.*, 2011, **133**, 11110.
55 H. Fei, C. H. Pham and S. R. J. Oliver, *J. Am. Chem. Soc.*, 2012, **134**, 10729.
56 L. Wenfeng, M. Hengchang and L. Ziqiang, *RSC Adv.*, 2014, **4**, 39351.
57 G. A. Crosby and J. N. Demas, *J. Phys. Chem.*, 1971, **75**, 991.
58 D. F. Sava Gallis, L. E. S. Rohwer, M. A. Rodriguez and T. M. Nenoff, *Chem. Mater.*, 2014, **26**, 2943.
59 L. Chen, J.-W. Ye, H.-P. Wang, M. Pan, S.-Y. Yin, Z.-W. Wei, L.-Y. Zhang, K. Wu, Y.-N. Fan and C.-Y. Su, *Nat. Commun.*, 2017, **8**, 15985.
60 C. Peng, X. Song, J. Yin, G. Zhang and H. Fei, *Angew. Chem., Int. Ed.*, 2019, **58**, 7818.
61 J. R. Lakowicz, *Principles of Fluorescence Spectroscopy*, Springer, US, 2007.
62 Y. Zhao, H. Zeng, X.-W. Zhu, W. Lu and D. Li, *Chem. Soc. Rev.*, 2021, **50**, 4484.
63 G. A. Leith, C. R. Martin, J. M. Mayers, P. Kittikhunnatham, R. W. Larsen and N. B. Shustova, *Chem. Soc. Rev.*, 2021, **50**, 4382.
64 K. Nakamoto, *Infrared and Raman Spectra of Inorganic and Coordination Compounds, Theory and Applications in Inorganic Chemistry*, Wiley, 1997.
65 N. Shen, Z. Yang, S. Liu, X. Dai, C. Xiao, K. Taylor-Pashow, D. Li, C. Yang, J. Li, Y. Zhang, M. Zhang, R. Zhou, Z. Chai and S. Wang, *Nat. Commun.*, 2020, **11**, 5571.
66 X. Li, H. Xu, F. Kong and R. Wang, *Angew. Chem., Int. Ed.*, 2013, **52**, 13769.
67 M. L. Schlegel, P. Reiller, F. Mercier-Bion, N. Barré and V. Moulin, *Geochim. Cosmochim. Acta*, 2006, **70**, 5536.
68 Y. S. Shimamoto and Y. Takahashi, *Anal. Sci.*, 2008, **24**, 405.
69 G. M. Sheldrick, *SADABS, program for empirical absorption correction of area detector data*; University of Göttingen, Göttingen, Germany, 1996.
70 G. M. Sheldrick, *Acta Crystallogr., Sect. A: Found. Adv.*, 2015, **71**, 3.
71 G. M. Sheldrick, *Acta Crystallogr., Sect. C: Struct. Chem.*, 2015, **71**, 3.
72 O. V. Dolomanov, L. J. Bourhis, R. J. Gildea, J. A. K. Howard and H. Puschmann, *J. Appl. Crystallogr.*, 2009, **42**, 339.
73 A. L. Spek, *Acta Crystallogr., Sect. C: Struct. Chem.*, 2015, **71**, 9.
74 H. S. Yu, X. J. Wei, J. Li, S. Q. Gu, S. Zhang, L. H. Wang, J. Y. Ma, L. N. Li, Q. Gao, R. Si, F. F. Sun, Y. Wang, F. Song, H. J. Xu, X. H. Yu, Y. Zou, J. Q. Wang, Z. Jiang and Y. Y. Huang, *Nucl. Sci. Tech.*, 2015, **26**, 50102.
75 B. Ravel and M. Newville, *J. Synchrotron Radiat.*, 2005, **12**, 537.
76 J. J. Rehr, J. J. Kas, F. D. Vila, M. P. Prange and K. Jorissen, *Phys. Chem. Chem. Phys.*, 2010, **12**, 5503.

© 2021 The Author(s). Published by the Royal Society of Chemistry